LAWRENCE
LIVERMORE
NATIONAL
LABORATORY

UCRL-JRNL-228449

Extracellular Proteins Limit the Dispersal of Biogenic Nanoparticles

J. W. Moreau, P. K. Weber, M. C. Martin, B. Gilbert, I. D. Hutcheon, J. F. Banfield

February 28, 2007

Science

Extracellular proteins limit the dispersal of biogenic nanoparticles

J.W. Moreau[1,*+], P.K. Weber[2], M.C. Martin[3], B. Gilbert[4],
I.D Hutcheon[2] and J.F. Banfield[1,5]

[1]Department of Earth and Planetary Science,
University of California Berkeley, Berkeley, CA, USA

[2]Glenn T. Seaborg Institute, Lawrence Livermore National Laboratory, Livermore, CA, USA

[3]Advanced Light Source, Lawrence Berkeley National Laboratory, Berkeley, CA, USA

[4]Earth Science Division, Lawrence Berkeley National Laboratory, Berkeley, CA, USA

[5]Department of Environmental Science, Policy, and Management, University of California Berkeley, Berkeley, CA, USA

* Current Address: United States Geological Survey Water Resources Division, 8505 Research Way, Middleton, WI, USA 53562

[+] Corresponding author: jwmoreau@usgs.gov

Summary: Proteins are trapped within dense aggregates of bacterially-formed metal sulfide nanoparticles, and may have played a key role in the aggregation process.

Micron-scale, concentrically-zoned spheroidal aggregates of biogenic zinc sulfide nanoparticles formed by sulfate-reducing bacteria in natural biofilms contain polypeptides or proteins. The previously unreported intimate association of peptide-rich organic matter with metal-sulfides is a form of extracellular biomineralization. Experiments involving synthetic ≤ 3 nm-diameter ZnS particles and a suite of representative amino acids indicate an important role for cysteine in driving rapid particle aggregation. The findings suggest that microbially-derived proteins can limit the dispersal of abundant nanometer-scale bioremediation products that otherwise may be transported by fluid flow in the subsurface.

Introduction

Sulfate-reducing bacteria (SRB) can lower the concentrations of metals in anoxic waters by sequestering metals into nanoparticles (e.g., *1-3*). However, these particles are potentially highly mobile due to their small size (*4*). The smallest particles are < 2 nm diameter, comparable to molecular clusters (*6*), while most are 2 to 6 nm (*2, 5*). Small size facilitates both transport and oxidative re-dissolution (*7, 8*). Aggregation can restrict transport by inducing settling of colloids from solution (*9, 10*), simultaneously promoting crystal growth and decreasing solubility (*11, 12*). Amine-bearing organic molecules have been shown to organize sulfide nanoparticles into semiconductor nanowires (*13*). In this study, we investigated the hypothesis that natural organic matter contributed to the

formation of densely-aggregated nanoparticulate ZnS spheroids, and remains preserved in nanometer-scale pores (*5*). We use microanalytical and direct isolation approaches to analyze nanoparticle aggregates formed in natural sulfate-reducing bacterial biofilms (*14*), and experimentally evaluate the potential for amino acids to induce the rapid aggregation of metal-sulfide nanoparticles.

We examined natural SRB-dominated biofilms collected from the Piquette Pb, Zn mine in southwestern Wisconsin, USA (*14*). Ultramicrotomed sections of biofilm containing spheroidal aggregates of biogenic ZnS nanoparticles (Figs. S1-S3) were imaged with transmission and scanning electron microscopy (TEM and SEM, respectively) prior to *in situ* isotopic microanalysis with high-resolution secondary ion mass spectrometry (NanoSIMS) at a spatial resolution of ~50 nm (*15*).

Comparison of TEM/SEM images with NanoSIMS ^{32}S isotope maps demonstrates that ZnS spheroids are the only structures within the biofilm that contain significant concentrations of sulfur. The composite NanoSIMS data show the intimate association of $^{12}C^{14}N$ with biofilm ZnS (Figs. 1, S7, S8) at significantly higher levels than in the abiotic ZnS reference materials (Fig. S5). Nitrogen is present throughout the biofilm ZnS aggregates. Pores in the ZnS aggregates appear as low diffraction-contrast features in TEM images, due to a lower concentration of sphalerite nanoparticles (Fig. S2). These porous regions are associated with the highest $^{12}C^{14}N$ intensities (N concentrations*;* Figs. S7, S8). In comparison, composite isotope maps of reference materials show that the nitrogen concentrations in synthetic ZnS aggregates are ~100x lower than in biofilm ZnS (Fig. S5). Based on an empirical relative sensitivity factor for N in ZnS, we estimate

from analysis of 134 ZnS spheroids an average nitrogen concentration of 1.60 wt% ± 0.22 (s.d.).

Nitrogen in the biofilm ZnS could be present as either an organic or inorganic form. Dissolved nitrate is present in mine waters at concentrations ~3 ppm, but this small amount should be removed from the biofilm during sample processing. We tested this hypothesis by analyzing the biofilm for $^{14}N^{16}O$, which yielded very low counts relative to $^{12}C^{14}N$ (*15*), indicating that N is not present as an oxidized species (e.g. nitrate, nitrite). The $^{12}C^{14}N^{-}/^{14}N^{16}O^{-}$ ratio in the biofilm and ZnS spheroids was compared to this ratio in a sample of KNO_3 in graphite as a nitrate reference (USGS-32 KNO_3 in graphite) and to bacterial spores as an organic nitrogen reference, to test for significant levels of nitrate in the ZnS spheroids. The $^{12}C^{14}N^{-}/^{14}N^{16}O^{-}$ ratio in the KNO_3 in graphite sample ranged from 1 to 150, with a weighted average of ~15. The $^{12}C^{14}N^{-}/^{14}N^{16}O^{-}$ ratio in the bacterial spores ranged from 2000 to 4000. The $^{12}C^{14}N^{-}/^{14}N^{16}O^{-}$ ratio in the biofilm and biofilm ZnS is 2000 to 3500. Based on these analyses, we conclude that nitrogen in the biofilm is not associated with oxygen and is organic in nature. This conclusion is further supported by the presence of amide absorption features in the infrared spectroscopy data below. We note that, from the N content of ZnS estimated above, and using an average amino acid N concentration ~11 wt%, the ZnS spheroids could contain as much as ~14 wt% amino acids.

Areas enriched in $^{12}C^{14}N$ with cell-like morphologies (Fig. 1) and increased ^{31}P content (data not shown) are interpreted as either whole or degraded microbial cells. These features are morphologically distinct compared to ZnS spheroids, arguing against spheroid formation by encrustation of microbes. We thus infer that the ZnS spheroids

formed by aggregation of ZnS nanoparticles generated by BSR with polypeptides or proteins. The process may have involved ZnS nanoparticles with surface adsorbed peptides or co-aggregation of protein molecules and nanoparticles.

Synchrotron-based Fourier-transform infrared spectroscopy (SR-FTIR), with ~10 um spatial resolution, was used to further classify organic molecules detected within aggregates (*15*). SR-FTIR analyses revealed that absorptions at both ~1,580 cm^{-1} and ~1,640 cm^{-1} are only associated with ZnS spheroid-rich regions of the biofilm (Fig. 2). Absorption features at ~1,580 cm^{-1} and ~1,640 cm^{-1} are assigned to amide II and amide I vibration modes, respectively, and are characteristic of polypeptide- and/or protein-derived amino acids (*17*). Analyses varied in the relative magnitudes of amide I and II absorption features by only a few percent. The SR-FTIR data confirm that $^{12}C^{14}N$ measured in NanoSIMS analyses of spheroid-rich regions of biofilm originate from polypeptides or proteins, and suggest that these regions contain increased concentrations of these components relative to spheroid-free regions.

Proteins were directly extracted (*15*) from density-separated fractions dominated by either organic biofilm components or ZnS spheroids (Fig. S6). Proteins from the biofilm fraction produce faint bands in 4-10% polyacrylamide gradient SDS gels at molecular weights of ~37 kDa and ~48 kDa (*15*; Fig. 3). In contrast, the ZnS-enriched fraction yielded a more predominant band at ~37 kDa, suggesting that the amino acids detected by NanoSIMS and SR-FTIR are associated with protein(s) of this molecular mass. It was not possible to identify this protein or group of proteins or to assess the degree of functionality or degradation state, due to the limited availability and accessibility (*14*) of sample. However, a size of 30 – 50 kDa is consistent with known

bacterial metal-binding proteins functionally similar to metallothionein (e.g., *17-19*). Recently, the SRB species *Desulfovibrio desulfuricans* and *Desulfococcus multivorans*, grown in media with Cd^{2+}, were shown to express genes homologous to *SmtA* (*20*), a gene coding for a protein required by *Synechococcus* for Zn^{2+} resistance (*21*). An unidentified extracellular metal-binding compound has also been partially purified from *D. multivorans* (*22*), a member of the family *Desulfobacteraceae*, one of two major SRB groups active within the biofilm (*14*). These similarities raise the interesting possibility that the ZnS-associated protein(s) found in this study may serve a similar function.

The low-density zones between concentric shells of densely packed ZnS nanoparticles (*5*) likely accommodate larger proteins and may represent peptide-rich organic-coatings that were adsorbed to aggregate surfaces between episodes of ZnS nanoparticle precipitation (e.g., resulting from seasonally controlled cycles of SRB activity). The high $^{12}C^{14}N$ regions surrounding the outermost surfaces of some aggregates may be protein-rich coatings that are the contemporary equivalent. Alternating bands of organics and ZnS may record temporal patterns of microbial activity.

In some aggregates NanoSIMS data indicate overlapping $^{12}C^{14}N$ and ^{32}S distributions, implying fine-scale mixtures of ZnS nanoparticles and protein-rich organic matter. Thus, a fraction of the amino acids may be bound to the surfaces of nanoparticles. Known bacterial metal-binding proteins bind zinc and other potentially toxic metals (e.g., Cd, Cu), primarily at cysteine residues in proximity to OH^- groups (*23*). Experimental evidence shows that (1) cysteine also binds strongly to ZnS nanoparticles and limits their size to < ~5 nm (*24*), and (2) thiol groups bind strongly with sulfur-deficient surface Fe(II) atoms in pyrite (FeS_2) (*25*). The conditional stability

constant for mono-ligand cysteine-Zn^{2+} complexation in low ionic strength solutions (≤ 0.1 M_c) at 20-25 °C is >4 orders of magnitude larger than those of all the other amino acids tested except for lysine, for which the constant is ~2 orders of magnitude larger (*15*). These observations suggest that cysteine or cysteine-rich polypeptides or metal-binding proteins could have played a role in determining the ZnS particle size and aggregation state.

We tested the efficacy of individual amino acids (100 μM of alanine, aspartate, cysteine, lysine, phenylalanine, proline, and serine) to promote aggregation of synthetic < 3 nm-sized ZnS (10 μM ZnS) (15). Aggregation was monitored periodically using dynamic light scattering (DLS; *15*). Results showed that the inorganic aggregation of ZnS occurred rapidly at first, to form ~100 nm-diameter aggregates, but then slowed greatly or ceased after one week (Figs. 4, S10). The dynamic light scattering for ZnS after one week of continuous reaction was ~5 x 10^4 counts per second (cps). In contrast, cysteine plus ZnS yielded ~8 x 10^4 cps, nearly twice that of ZnS alone, and a direct indication of the presence of larger aggregates in solution. Cysteine also prolonged the aggregation process; after one week the average aggregate size continued to increase, ultimately forming 1-10 μm-sized structures. Other amino acids had little (e.g., serine, lysine) to no (e.g., alanine, phenylalanine) detectable effect on nanoparticle aggregation. Cysteine in the absence of ZnS produced ~3 x 10^4 cps and formed no measurable aggregates (data not shown). Humic compounds added to ZnS nanoparticle suspensions did not accelerate aggregation. In conclusion, the effect of cysteine on ZnS nanoparticle aggregation rate and final aggregate size is pronounced relative to that of other amino

acids or ZnS nanoparticles alone. Our experimental results suggest a role for cysteine or cysteine-bearing molecules in biofilm ZnS spheroid formation.

Mineral-protein mixtures with internal organization are typically considered biominerals, and biominerals normally form within organisms. The structures reported here represent an exception to this pattern. Proteins, peptides, and amino acids could be released after cell death and scavenged by hydrophobic ZnS surfaces. Alternatively, bacteria may export Zn-binding proteins for a physiological reason. Most known bacterial metal-binding proteins are produced for intracellular binding and subsequent export of toxic metals (*23*). In the case reported here, exported metal-binding proteins may promote aggregation-induced "clearing" (*26*) of very small and potentially toxic (*27*) metal-sulfide nanoparticles from the biofilm solution, preventing incidental uptake into cells (e.g., *28*) and/or cell entombment. Hydrophobic interactions among peptide/protein-ZnS complexes may have induced formation of dense (rather than open, fractal-like) aggregates, and led to the observed spheroidal morphology. Densely packed aggregates of metal-bearing nanoparticles, similar to the biofilm ZnS spheroids characterized in this study, have been reported in other metals-contaminated systems (e.g., *39*). Similar aggregates may be present in sediments, where they could trap and preserve organic molecules.

There is a growing body of evidence for both nanoparticle-based contaminant transport (*1-5*) and trapping of nanoparticles in the vicinity of their formation site (*30*). Our results suggest that metal-binding polypeptides and proteins play a key, and previously unrecognized, role in extracellular metal-sulfide biomineralization, and may be an important factor limiting nanoparticle dispersal in natural environments.

Acknowledgements

We thank Rick and Robyn Webb (University of Queensland, Australia), Hengzhong Zhang (University of California, Berkeley), and Christina Ramon (Lawrence Livermore National Laboratory, LLNL) for invaluable assistance in acquiring or preparing biofilm and synthetic ZnS samples for TEM and NanoSIMS, and Michael Thelen and Chris Jeans (LLNL) for assistance with protein extractions. Work was funded by the U.S. Department of Energy Basic Energy Sciences Program under Contract no. DE-FG02-04ER15507, the NASA Astrobiology Institute under Contract no. NNA04CC02A (JWM and JFB), and the U.S. Department of Energy Office of Biological and Environmental Research Genomics: GTL research program (PKW and IDH). Work performed at UC, LLNL under the auspices of the U.S. Department of Energy under Contract no. W-7405-Eng-48. The Advanced Light Source is supported by the Director, Office of Science, Office of Basic Energy Sciences, of the U.S. Department of Energy under Contract no. DE-AC02-05CH11231.

References

1. Lloyd, J.R., Mabbett, A.N., Williams, D.R. and Macaskie, L.E. (2001) Metal reduction by sulphate-reducing bacteria: physiological diversity and metal specificity. *Hydrometallurgy*, 59, 327-337.

2. Suzuki, Y., Kelly, S.D., Kemner, K.M., and Banfield, J.F. (2002) Nanometre-sized products of uranium bioreduction. *Nature*, 419, 134.

3. Hockin, S.L. and G.M. Gadd (2003) Linked redox precipitation of sulfur and selenium under anaerobic conditions by sulfate-reducing bacteria. *Applied and Environmental Microbiology*, 69, 7063-7072.

4. Honeyman, B.D. (1999) Colloidal culprits in contamination. *Nature*, 397, 23-24.

5. Moreau J. W., Webb R. I. and Banfield J. F. (2004) Ultrastructure, aggregation-state, and crystal growth of biogenic nanocrystalline sphalerite and wurtzite. *American Mineralogist* 89, 950-960.

6. Luther, G.W., S.M. Theberge and D.T. Rickard (1999). Evidence for aqueous clusters as intermediates during zinc sulfide formation. *Geochimica. et Cosmochimica. Acta*, 63, 3159-3169.

7. Evangelou, V.P. and Zhang, Y.L. (1995) A review: pyrite oxidation mechanisms and acid mine drainage prevention. *CRC Critical Reviews in Environmental Control*, 25, 141-199.

8. Edwards, K.J., Bond, P.L., Druschel, G.K., McGuire, M., Hamers, R.J., and Banfield, J.F. (2000) Geochemical and biological aspects of sulfide mineral dissolution: lessons from Iron Mountain, California. *Chemical Geology*, 169, 383-397.

9. Dietrich, W.E. (1982) Settling velocity of particles. *Water Resources Research*, 18, 1615-1626.

10. Johnson, C.P., Li, X., and Logan, B.E. (1996) Settling velocities of fractal aggregates. *Environmental Science and Technology*, 30, 1911-1918.

11. Zhang, J.W. and Nancollas, G.H. (1990) Mechanisms of growth and dissolution of sparingly soluble salts. In Hochella, Jr., M.F. and White, A.F. (Eds.) Mineral-water interface geochemistry. *Reviews in Mineralogy and Geochemistry*, 23, 365-393.

12. Stumm, W. and Morgan, J.J. (1996) Aquatic chemistry: chemical equilibria and rates in natural waters. pp. 400-414, Wiley and Sons, New York, 1022 pp.

13. Lu, Q., Gao, F., and Zhao, D. (2002) The Assembly of semiconductor sulfide nanocrystallites with organic reagents as templates. *Nanotechnology*, 13, 741-745.

14. Labrenz M., Druschel G. K., Thomsen-Ebert T., Gilbert B., Welch S. A., Kemner K. M., Logan G. A., Summons R. E., De Stasio G., Bond P. L., Lai B., Kelly S. D. and Banfield J. F. (2000) Formation of sphalerite (ZnS) deposits in natural biofilms of sulfate-reducing bacteria. *Science* 290, 1744-1747.

15. Materials and methods are available as supporting material on *Science* Online.

16. Bebie, J., Schoonen, M.A.A., Fuhrmann, M. and Strongin, D.R. (1998) Surface charge development on transition metal sulfides: an electrokinetic study. *Geochimica et Cosmochimica Acta*, 62, 633-642.

17. Khazaeli, M.B. and Mitra, R.S. (1981) Cadmium-binding component in *Escherischia coli* during accomodation to low levels of this ion. *Applied and Environmental Microbiology*, 41, 46-50.

18. Kurek, E., Francis, A.J. and Bollag, J.M. (1991) Immobilization of cadmium by microbial extracellular products. *Archives of Environmental Contamination and Toxicology*, 20, 106-111.

19. Nies, D.H. (1992) CzcR and CzcD, gene products affecting regulation of resistance to cobalt, zinc, and cadmium (*czc* sytem) in *Alcaligenes eutrophus*. *Journal of Bacteriology*, 174, 8102-8110.

20. Naz, N., Young, H.K., Ahmed, N. and Gadd, G.M. (2005) Cadmium accumulation and DNA homology with metal resistance genes in sulfate-reducing bacteria. *Applied and Environmental Microbiology*, 71, 4610-4618.

21. Blindauer, C.A., Harrison, M.D., Parkinson, J.A., Robinson, A.K., Cavet, J.S., Robinson, N.J. and Sadler, P.J. (2001) A Metallothionein containing a zinc finger within a four-metal cluster protects a bacterium from zinc toxicity. *Proceedings of the National Academy of Sciences*, 98, 9593-9598.

22. Bridge, T.A.M., White, C. an Gadd, G.M. (1999) Extracellular metal-binding activity of the sulphate-reducing bacterium *Desulfococcus multivorans*. *Microbiology*, 145, 2987-2995.

23. Rosen, B.P. (1996) Bacterial resistance to heavy metals and metalloids. *Journal of Biological Inorganic Chemistry*, 1, 273-277.

24. Torres-Martinez, C.L., Nguyen, L., Kho, R., Bae, W., Bozhilov, K., Klimov, V. and Mehra, R.K. (1999). Biomolecularly capped uniformly sized nanocrystalline materials: glutathione-capped ZnS nanocrystals. *Nanotechnology*, 10, 340-354.

25. Bebie, J. and Schoonen, M.A.A. (2000) Pyrite surface interaction with selected organic aqueous species under anoxic conditions. *Geochemical Transactions*, 8 (electronic article).

26. Feeney, R., Schmidt, S.L., Strickholm, P., Chadam, J., and Ortoleva, P. (1983) Periodic precipitation and coarsening waves: Applications of the competitive growth model. *Journal of Chemical Physics*, 78(3), 1293-1311.

27. Barkay, T. and Schaefer, J. (2001) Metal and radionuclide bioremediation: issues, considerations and potentials. *Current Opinion in Microbiology*, 4, 318-323.

28. Kloepfer, J.A., Mielke, R.E. and Nadeau, J.L. (2005) Uptake of CdSe and CdSe/ZnS quantum dots into bacteria via purine-dependent mechanisms. *Applied and Environmental Microbiology*, 71, 2548-2557.

29. Ahn, J.S., Park, Y.S., Kim, J.Y. and Kim, K.W. (2005) Mineralogical and geochemical characterization of arsenic in an abandoned mine tailings of Korea. *Environmental Geochemistry and Health*, 27, 147-157.

30. Anderson, R.T., Vrionis, H.A., Ortiz-Bernad, I., Resch, C.T., Long, P.E., Dayvault, R., Karp, K., Marutzky, S., Metzler, D.R., Peacock, A., White D.C., Lowe, M, and Lovley, D.R. (2003) Stimulating the in situ activity of *Geobacter* species to remove uranium from the groundwater of a uranium-contaminated aquifer. Applied and Environmental Microbiology, 69, 5884-5891.

Figure Captions:

Figure 1: NanoSIMS secondary ion images showing ^{12}C, $^{12}C^{14}N$ and ^{32}S in ultramicrotomed TEM section of biofilm and spheroidal ZnS aggregates. (**A**) Composite isotope map of ^{12}C (blue), $^{12}C^{14}N$ (green), and ^{32}S (red) for ~10 μm x 10 μm region of biofilm (area "C2.9"). Secondary and tertiary colors vary in hue and intensity to reflect relative proportions of two or three isotopic components, respectively. (**B**) *Box* key to color-coded isotopic distributions seen in (A); e.g. in (A), uniformly red spherules are relatively pure ZnS, while orange or yellow halos surrounding some spherules indicate enhanced levels of nitrogen. The key is projected through the ternary end member that would represent a combination of maximum ^{12}C, $^{12}C^{14}N$ and ^{32}S counts (i.e. through "white"). **(C)** SEM image of biofilm and ZnS spheroids in part of the region shown in (A). White arrows point to the same individual spheroids in (A) and (C) for reference. Scale bars =1μm.

Figure 2. SR-FTIR transmission spectra of biogenic ZnS aggregates (black) and background biofilm (grey). Amide I (~1640 cm^{-1}) and II (~1580 cm^{-1}) absorption features are diagnostic of amino-acid associated bond vibrations in polypeptides and/or proteins.

Figure 3: Composite SDS-PAGE gel electrophoresis image of biofilm and ZnS protein extractions. SyproOrange and colloidal silver molecular weight standards (far left and right lanes, respectively). (**A**) Extraction from the biofilm organic fraction

stained with SyproOrange. (**B**) Extraction of the ZnS spheroid fraction stained with SyproOrange. (**C and D**) Replicate extractions of biofilm organic fraction stained with silver. (**E and F**) Replicate extractions of ZnS spheroids fraction stained with silver. Numbers are molecular masses in kDa.

Figure 4: Size distribution curves from dynamic light scattering (DLS) data acquired in ZnS nanoparticles aggregation experiments. (**A**) Control experiments. 10 uM ZnS nanoparticles alone (solid lines) aggregate within 1 day to form ~100 nm radius clusters that exhibit little further growth over the 5 day period. 100 μM cysteine alone (dashed lines) gives a very weak DLS signal with is no consistent trend in size distribution. (**B**) In the presence of both 10 μM ZnS and 100 μM cysteine, sustained aggregation occurs over the 7 day period, resulting in aggregates that are more than 1 order of magnitude larger than the initial clusters. DLS correlation functions from which size distributions were derived are shown in Fig. S9.

Figure 1

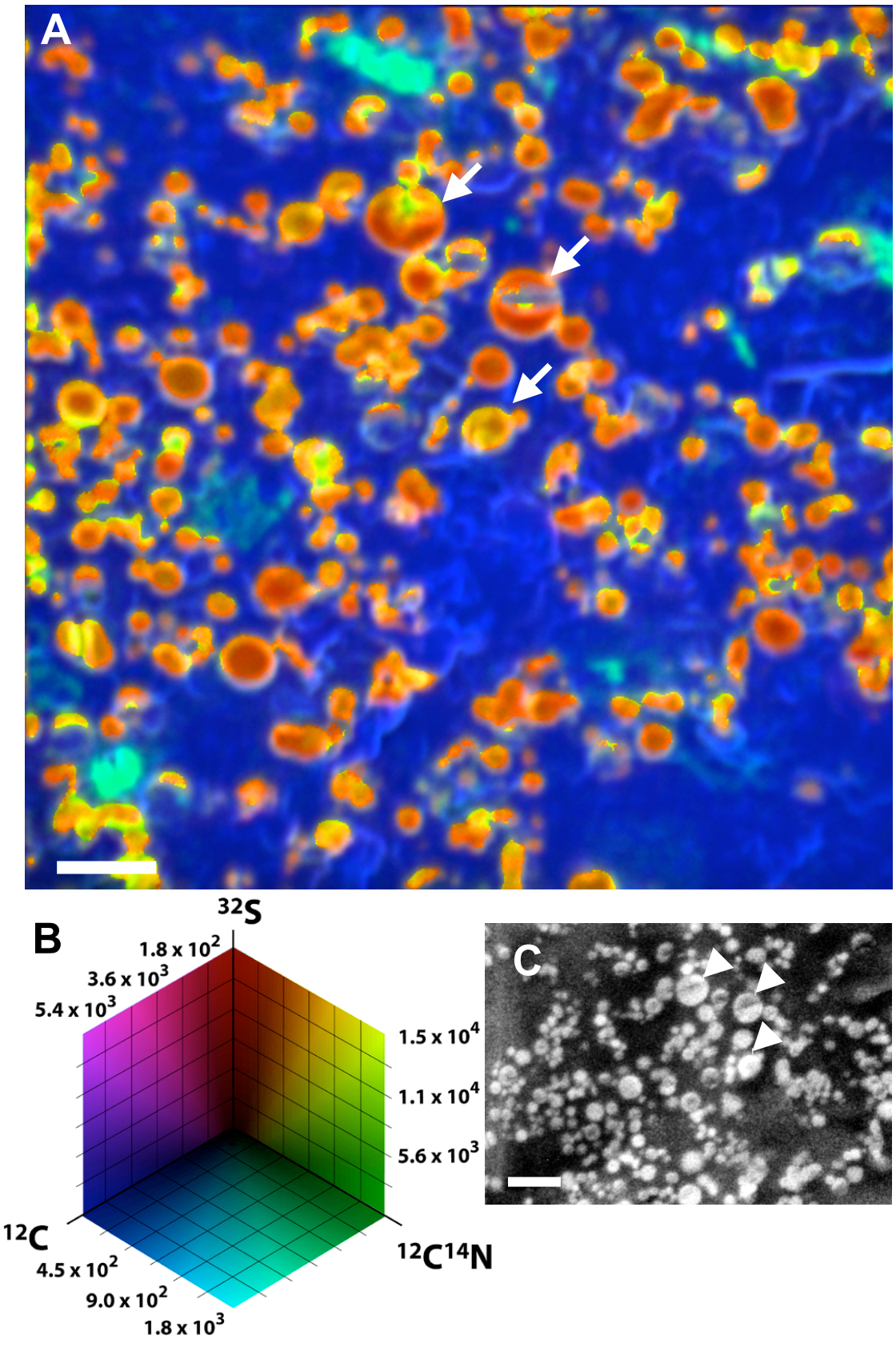
A
B
32S
1.8 x 10^2
3.6 x 10^3
5.4 x 10^3
12C
4.5 x 10^2
9.0 x 10^2
1.8 x 10^3
1.5 x 10^4
1.1 x 10^4
5.6 x 10^3
12C14N
C

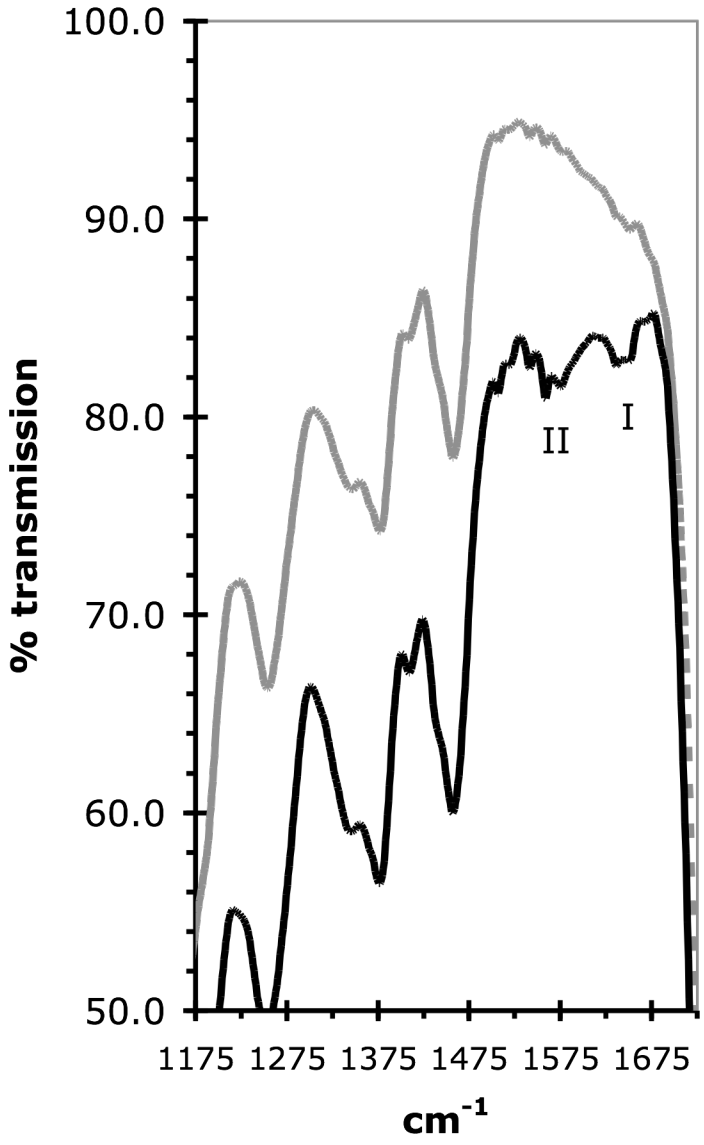
100.0
90.0
80.0
70.0
60.0
50.0
% transmission
II
I
1175 1275 1375 1475 1575 1675
cm-1

Figure 2

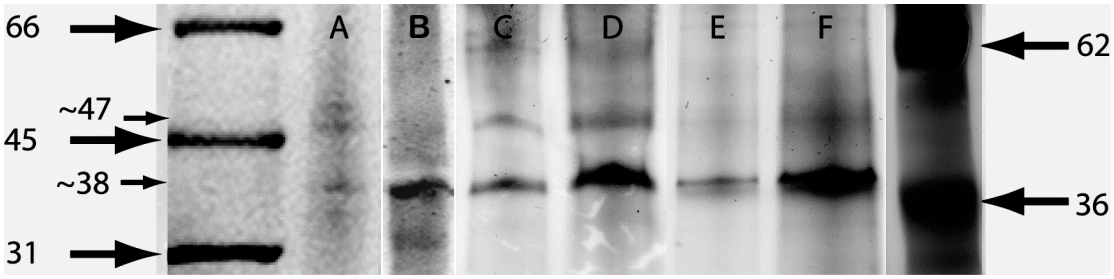

Figure 3

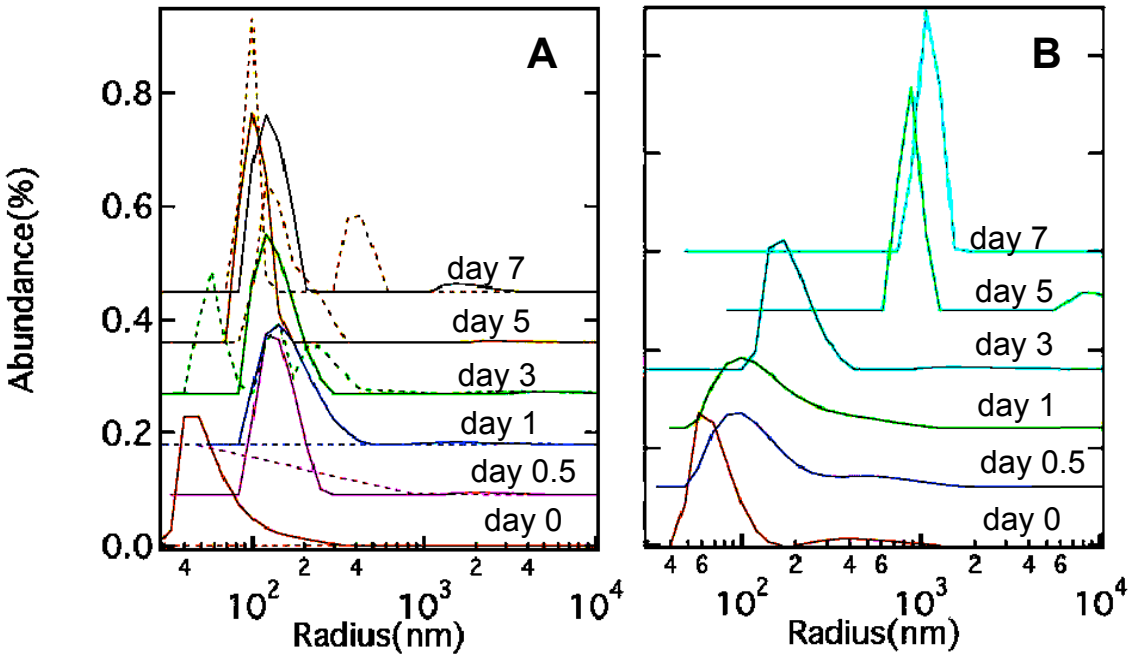
A
B
Abundance(%)
0.0
0.2
0.4
0.6
0.8
day 7
day 5
day 3
day 1
day 0.5
day 0
Radius(nm)
10^2
10^3
10^4

Figure 4

Supplementary Materials and Methods:

TEM/NanoSIMS biofilm sample preparation:

Samples of biofilm were fixed with 4% glutaraldehyde, as described previously (*1*). TEM images (Fig. S4) confirm that, because the sectioning resin neither displaces nor damages fine-scale biofilm features, ultramicrotomed samples of biofilm used for TEM imaging were also suitable for NanoSIMS analyses.

Secondary Ion Mass Spectrometry (SIMS):

SIMS was performed using the Lawrence Livermore National Laboratory NanoSIMS 50 (Cameca, Gennevilliers Cedex, France). The measurements were made with a 0.2 to 0.7 pA, 16 keV $^{133}Cs^+$ primary ion beam focused into a 50 to 100 nm diameter spot, rastered over sample areas of ~10 x 10 μm^2. The isotope imaging measurements consist of 15 to 100 replicate scans of 256 x 256 or 512 x 512 pixels with dwell times of 1-2 ms/pixel. Secondary ion intensities were collected simultaneously in multi-collection mode using three different collector configurations, [$^{12}C^-$, $^{12}C^{14}N^-$, $^{31}P^-$, $^{32}S^-$, $^{34}S^-$], [$^{12}C^-$, $^{12}C^{14}N^-$, $^{14}N^{16}O^-$, $^{32}S^-$, $^{14}N^{32}S^-$] and [$^{12}C^-$, $^{12}C^{14}N^-$, $^{32}S^-$, $^{34}S^-$, $^{14}N^{32}S^-$]. A mass resolving power of ~4000 was used. Samples were also simultaneously imaged using secondary electrons. Nitrogen concentration in the ZnS aggregates was estimated based on a relative sensitivity factor for NS^- (RSF_{NS}) in ZnS of 4.2 x 10^{24} cm^{-3} (*2*). The atom abundance of N per cm^3 of ZnS (C_N) is estimated from:

$$C_N = RSF_{NS} * I_{NS}/I_S,$$

where I_{NS} and I_S are the isotope corrected ion count rates for NS^- and S^- (*3*). The mass abundance of N per mass ZnS is calculated from C_N, Avogadro's number, the atomic mass of N and the density of ZnS. $^{12}C^{14}N^-$ is used in the presented images because it has a ~100x higher ion yield than $^{14}N^{32}S^-$ and therefore provides higher clarity images. Composite multi-isotope image maps were constructed using Photoshop and the NanoSIMS data analysis software, *L'image* (developed by L. Nittler, Carnegie Institution of Washington, Washingon, DC, USA). Grey-scale $^{12}C^-$, $^{12}C^{14}N^-$ and $^{32}S^-$ intensity images generated by *L'image* were assigned to blue, green and red channels, respectively, in Photoshop RGB image files. Primary colors in accompanying image map keys represent single isotope concentrations, whereas secondary or tertiary colors represent mixtures of two of three isotopic components. Black spots indicate areas of no data (i.e. holes in the TEM section). The significance of measurements obtained via NanoSIMS analyses of biofilm ZnS was determined by comparison to NanoSIMS analyses of natural and synthetic ZnS reference materials (Fig. S5) for > 1,000 regions-of-interest (ROIs) of ~180 nm^2 each. In addition to a natural single-crystal ZnS standard (Balmat sphalerite, NBS123), nanoparticulate ZnS synthesized by H. Zhang (UC Berkeley) was used to represent a similarly structured (i.e., nanocrystalline) pure ZnS reference material (*4*) for comparison.

Synchrotron-radiation Fourier transform infra-red spectroscopy (SR-FTIR):

SR-FTIR is capable of detecting and differentiating amongst nucleic acids, lipids, amino acids, and polysaccharides (*5*). The spatial resolution of SR-FTIR, coupled with optical microscopy, is diffraction limited, or between 2 and 10 μm in the mid-infrared (*6*). SR-FTIR analyses were conducted on uncoated ultramicrotomed sections of the same biofilm samples used for NanoSIMS analyses. The location of the synchrotron probe relative to targets selected with optical microscopy was calibrated using IR-sensitive targets on standards. Background spectra were obtained and used as reference spectra for both samples and standards to remove atmospheric H_2O and CO_2 absorptions.

Biofilm/ZnS separation and total protein extraction:

Biofilm samples were homogenized by repeated pipetting action through a series of sterile syringe needles of increasingly smaller inner-bore diameter (18-, 21- and 22-gauge, respectively, for approximately 20 minutes each). Homogenized biofilm slurries were then pelleted by centrifugation, re-suspended in lithium polytungstate solution (LST) of density ~2.8 g cm^{-3} (Geoliquids, Prospect Heights, IL, USA), and then subjected to further low-speed centrifugation (~5 mins at 1000 rpm) in autoclaved microcentrifuge tubes (Eppendorf, Hamburg, Germany). ZnS-rich biofilm fragments (ρ~4.1 g cm^{-3}) were easily pelleted at the bottom of LST-filled tubes during centrifugation, while ZnS-poor biofilm fragments rose to the top of the LST solution to be re-pipetted into new tubes. This process of low-speed centrifugation, density-based fractionation, collection and re-suspension was repeated several times, until no further separation of ZnS-rich and ZnS-poor biofilm fractions was observed. Both fractions were transferred a final time by pipette to clean tubes of nuclease-free water, and then pelleted, washed and re-suspended 6-8 times, to remove all traces of LST. Each resulting fraction represents a subsample of biofilm or ZnS spheroids with greatly increased relative concentrations of organic matter or ZnS, respectively. This method avoids the use of surfactants or solvents that might solubilize and destroy organic biomolecules, including nucleic acids and proteins. Each "density fraction" from the separation process was pelleted and re-suspended a final time in 2% sodium dodecyl sulfate (SDS) solution for one hour at room temperature with gentle mixing to denature any proteins (*7*).

Protein gel electrophoresis:

Molecular weight standard "ladders" were run on both sides of all sample gel lanes to correct for horizontal distortions commonly produced during gel electrophoresis. Protein extractions were analyzed using two different molecular weight ladders and two different staining methods, for comparison of sample protein size/weights and staining efficiencies. One set of gels was reacted with a silver-based stain (Bio-Rad, Solano, CA, USA), after the method of Gottlieb and Chavko (*8*), and Kaleidoscope (Bio-Rad) pre-

stained molecular weight ladders were used to calibrate the weight/size of protein bands. These gels were imaged using a standard Epson scanner. The second set of gels was stained with SyproOrange, a UV-fluorescent dye that specifically binds to proteins (*9*), and protein bands were calibrated to broad-range SyproOrange molecular weight ladders. These gels were imaged using a UV-VIS light gel documentation system (Bio-Rad). Both SyproOrange and silver staining can be used to detect ≤10 ng of protein (Bio-Rad, written communication).

ZnS nanoparticle synthesis:

Nano-ZnS was synthesized by the reaction of 150 mM $ZnCl_2$ and aqueous sulfide, which were dissolved separately into 200 ml of ultra-pure (0.1 μm pore-size double-filtered MilliQ; Millipore, Billerica, MA, USA) DI water and reacted drop wise under constant stirring for 1.5 hr (*4*).

ZnS nanoparticle/amino acid aggregation experiments:

The initial size of ZnS precipitates was determined to be ≤ 3 nm diameter using a UV-vis spectrometer (Ocean Optics, Dunedin, FL, USA) calibrated for ZnS particle size using published TEM observations (*10*). The following experimental conditions were established in separate glass flasks: (a) "blanks" (ultrapure water only), (b) ZnS nanoparticles only, (c) a single amino acid only and (d) ZnS nanoparticles plus a single amino acid. All incubation flasks were (in the following order) detergent-washed, rinsed with MilliQ water three times, acid-washed in 0.1N HCl overnight, rinsed five times with MilliQ water, and sealed with parafilm, prior to the experiment. After the addition of any reagents, flasks were resealed with parafilm and kept sealed during the experiment between sampling times. All flasks were gently stirred throughout the experiment by acid-washed Teflon-coated magnetic stirrer bars. 1 ml aliquots from each experimental condition were taken at 0, 0.5, 1, 3, 5, and 7 days of reaction progress. Between sample measurements, 0.5 ml of 0.1 N HCl was flushed through the sample line and chamber, followed by 3 ml of ultrapure water, to avoid cross-contamination of samples. Three measurements of 40 – 60 accumulations each were obtained per analysis at each sampling time point.

The amino acids chosen for these aggregation experiments represent the following classes of structures and functional groups: alanine (nonpolar, aliphatic), aspartate (acidic, negatively charged), cysteine (polar, uncharged, thiol-bearing), lysine (basic, positively charged), phenylalanine (aromatic), proline (polar, uncharged, imine-bearing), and serine (polar, uncharged, hydroxyl-bearing). Their conditional stability constants for mono-ligand complexation of aqueous Zn^{2+} are given in Table 2, from data collected by Martell and Smith (*11*).

Dynamic light scattering analysis (DLS):

DLS analysis was performed with a PD-Expert Workstation (Precision Detectors, Bellingham, MA, USA) fitted with a quartz flow-through cell maintained at 25 °C. Laser

light (685 nm wavelength) scattered through 135° was sent via glass fiber to an optical correlator. The DLS correlation function is a direct measurement of the diffusion coefficient(s) of objects suspended in a solvent. For specific values of solvent viscosity and refractive index, an effective hydrodynamic radius, R_H, of the object(s) can be calculated (*12*). In the present case, we observed light scattering from aggregates of ZnS nanoparticles. Because the exact shape and hydrodynamic properties of nanoparticulate aggregates are not well known, there may be systematic differences between the calculated R_H and spatial dimensions observed by alternative techniques (such as electron microscopy). Determination of the distribution of ZnS aggregate sizes was performed using proprietary Precision Detectors software (PrecisionDeconvolve) that employs a regularization algorithm (*13*) to seek a smooth, non-negative size distribution function that provides the best fit to the data. Low noise DLS data analyzed with this method can resolve multimodal distributions, provided the diffusion coefficients differ by greater than a factor of ~ 2.5.

Supplementary References:

1. Moreau J. W., Webb R. I. and Banfield J. F. (2004) Ultrastructure, aggregation-state, and crystal growth of biogenic nanocrystalline sphalerite and wurtzite. *American Mineralogist* 89, 950-960.

2. private communication, Robert G. Wilson, December 30, 2006

3. Wilson, R. G., Stevie, F. A. and Magee, C. W. (1899) Secondary Ion Mass Spectrometry: A Practical Handbook for Depth Profiling and Bulk Impurity Analysis**.** Wiley, New York.

4. After the method of Müller, B.R., Majoni, S., Memming, R. and Meissner, D. (1997) Particle-size and surface chemistry in photoelectrochemical reactions at semiconductor particles. Journal of Physical Chemistry B, *101*, 2501-2507.

5. Mantsch, H.H. and Chapman, D. (1996) Infrared spectroscopy of biomolecules. Wiley-Liss, New York. 359 pp.

6. Levenson, E., Lerch, P. and Martin, M.C. (2006) Infrared Imaging: Synchrotrons vs. Arrays, Resolution vs. Speed. Infrared Physics and Technology, 49, 45-52.

7. Following the method of Sambrook, J., Fritsch, E.F. and Maniatis, T. (1989) Molecular cloning: a laboratory manual. 2nd. Ed., Cold Spring Harbor Laboratory Press, Cold Spring Harbor.

8. Gottlieb, M. and Chavko, M. (1987) Silver staining of native and denatured eucaryotic DNA in agarose gels. *Analytical Biochemistry*, 165, 33-37.

9. Lawrence, J.R., Swerhone, G.D.W., Leppard, G.G., Araki, T., Zhang, X., West, M.M. and Hitchcock, A.P. (2003) Scanning transmission x-ray, laser scanning, and transmission electron microscopy mapping of the exopolymeric matrix of microbial biofilms. *Applied and Environmental Microbiology*, 69, 5543-5554.

10. Zhang, H., Gilbert, B. Huang, F., and Banfield, J.F. (2003) Water-driven transformation of nanoparticle structure at room temperature. *Nature*, 424, 1025-1029.

11. Martell, A.E. and Smith, R.M. (1974) Critical stability constants, vol. 1: amino acids. Plenum Press, New York.

12. Romer, S., Urban, C., Lobaskin, V., Scheffold, F., Stradner, A., Kohlbrecher, J. and Schurtenberger, P. (2003) Simultaneous light and small-angle neutron scattering on aggregating concentrated colloidal suspensions. *Journal of Applied Crystallography*, 36, 1-6.

13. Provencher SW (1982) CONTIN - A general-purpose constrained regularization program for inverting noisy linear algebraic and integral-equations. Computer Physics Communications, 27, 229-242.

Supplementary Figure Captions:

Figure S1: Field-emission scanning electron microscopy (FESEM) secondary electron image of micron-scale spheroidal aggregates of nanocrystalline biogenic ZnS formed in the biofilm. Scale bar is 2 um.

Figure S2: HRTEM image of cross-section through spheroidal biogenic ZnS aggregate in the biofilm. Multiple concentric rings (3-5 nm wide, shown by white arrows) of low electron density attributed to porous regions separate bands of densely aggregated nanoparticulate ZnS.

Figure S3: High-resolution transmission electron microscopy (HRTEM) images of biogenic ZnS nanoparticles formed in a biofilm of sulfate-reducing bacteria. (**A**) The smallest ZnS nanoparticles are crystalline, as shown by {111} lattice fringes in [02-2] projection, and <2 nm-diameter. (**B**) Several aggregated nanoparticles with boundaries indicated by dashed lines. (**C**) Disordered ZnS aggregates contain multiple stacking faults (interpolated along pairs of white lines) that give rise to wurtzite subdomains (across white line pairs) in sphalerite. (**D**) Example of aggregation producing faceted surfaces and negative crystals (dashed white triangle). All scale bars are 2 nm.

Figure S4: **TEM image of biofilm organic matter, cells and ZnS aggregates.** Stained ultramicrotomed sections of biofilm show abundant ZnS spheroidal aggregates (black spheroidal features with strong diffraction contrast) surrounded by biofilm organic matter

(white arrows), and in close proximity to cells (black arrows). Dark grey spheroidal features with lighter grey cores (grey arrows) are cells surrounded by capsular organic matter that has been stained with uranyl acetate and lead citrate. Scale bars are 1μm.

Figure S5: NanoSIMS secondary ion images showing ^{12}C, $^{12}C^{14}N$ and ^{32}S isotopic distributions in ultramicrotomed TEM section of standard reference materials. (**A**) Composite isotope map of ^{12}C (blue), $^{12}C^{14}N$ (green), and ^{32}S (red) in ultramicrotomed Balmat sphalerite. Secondary and tertiary colors vary in hue and intensity to reflect relative proportions of two or three isotopic components, respectively. **(B)** Composite isotope map of ultramicrotomed synthetic ZnS aggregates. $^{12}C^{14}N$ maximum counts are ~200 in both (A) and (B), and are 2-3 orders of magnitude lower than the same intensity in biofilm samples. (**C**) *Box* key to color-coded isotopic distributions seen in (A) and (B). The key is projected through the ternary end member that would represent a combination of maximum ^{12}C, $^{12}C^{14}N$ and ^{32}S counts (i.e. through "white"). Scale bars =1μm.

Figure S6: **Microcentrifuge tubes of lithium-polytungstate solution (LST), biofilm and ZnS.** The left-hand tube shows the color of pure LST. Homogenized biofilm is introduced and subjected to low speed centrifugation to separate lower and higher density fractions (middle tube). Density-driven separation is iteratively repeated until no further separation is achieved (right-hand tube). Material at the top of the LST solution consists predominantly of biofilm organic matter, while the pellet at the bottom is concentrated in ZnS spheroids.

Figure S7: NanoSIMS secondary ion images showing ^{12}C, $^{12}C^{14}N$ and ^{32}S isotopic distributions in ultramicrotomed TEM section of biofilm and spheroidal ZnS aggregates. (**A**) Composite isotope map of ^{12}C (blue), $^{12}C^{14}N$ (green), and ^{32}S (red) in biofilm area "D6.2". Secondary and tertiary colors vary in hue and intensity to reflect relative proportions of two or three isotopic components, respectively. *(**B**) Box* key to color-coded isotopic distributions seen in (A) and (C). The key is projected through the ternary end member that would represent a combination of maximum ^{12}C, $^{12}C^{14}N$ and ^{32}S counts (i.e. through "white"). **(C)** TEM image of biofilm and ZnS spheroids in partial field of view from (A). Scale bars =1μm.

Figure S8: NanoSIMS secondary ion images showing ^{12}C, $^{12}C^{14}N$ and ^{32}S isotopic distributions in ultramicrotomed TEM section of biofilm and spheroidal ZnS aggregates. (**A**) Composite isotope map of ^{12}C (blue), $^{12}C^{14}N$ (green), and ^{32}S (red) in biofilm area "D6.3". Secondary and tertiary colors vary in hue and intensity to reflect relative proportions of two or three isotopic components, respectively. *Color wheel*: key to isotopic distributions. (**B**) *Box* key to color-coded isotopic distributions seen in (A) and (C). **(C)** TEM image of biofilm and ZnS spheroids in partial field of view from (A). Scale bars =1 μm.

Figure S9: Dynamic light scattering (DLS) correlation functions acquired during ZnS nanoparticle aggregation experiments: (**A**) 100 μM cysteine, (**B**) 10 μM ZnS, (**C**)

10 μM ZnS and 100 μM cysteine. A trend in the data indicating continuous aggregation was observed only for the sample containing both ZnS and cysteine. For this sample, the scattering intensity increased (improving data quality) and there was a steady trend in the correlation function threshold indicating the formation of larger suspended aggregates.

Supplementary Figures:

Figure S1

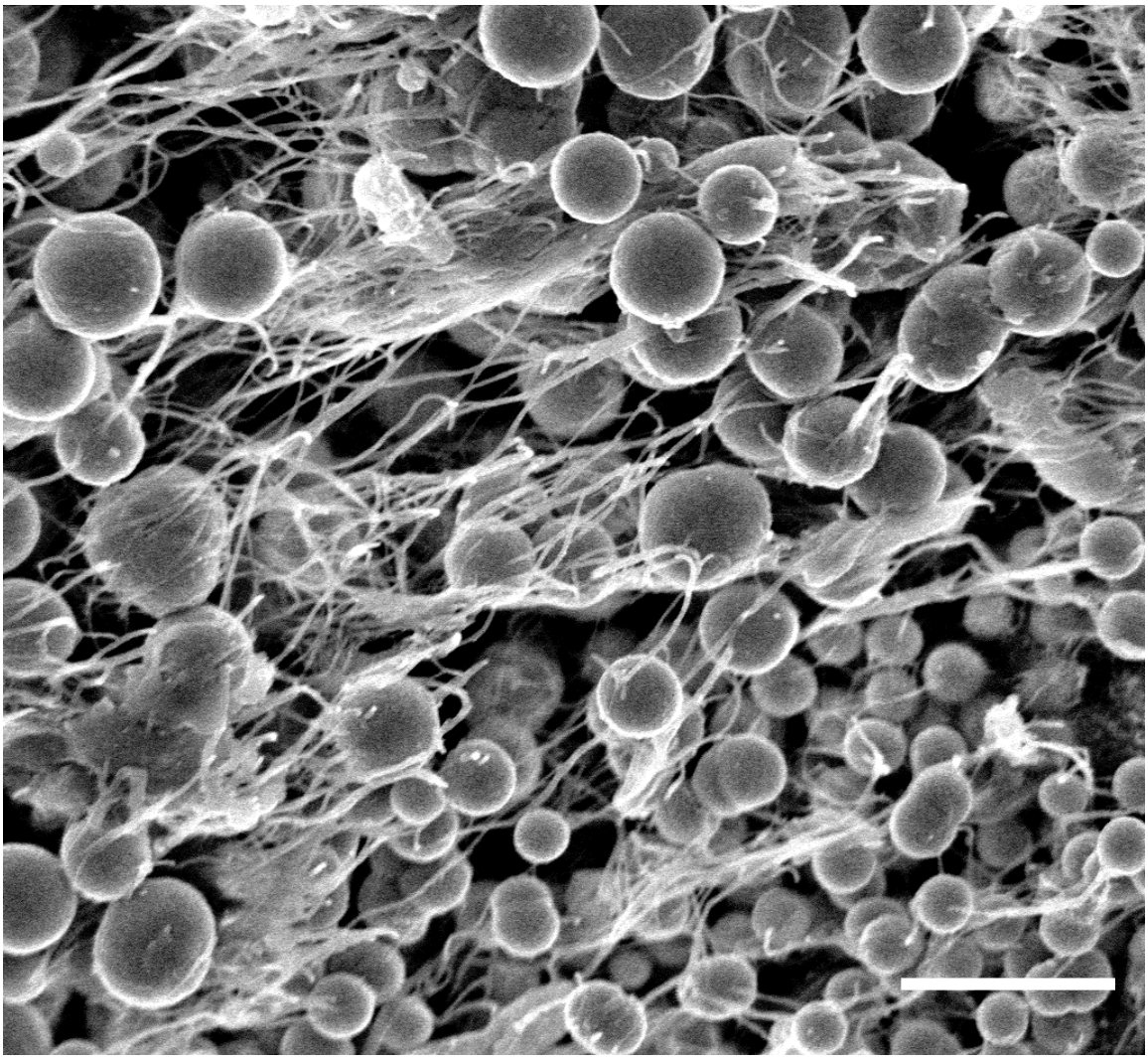

Figure S2

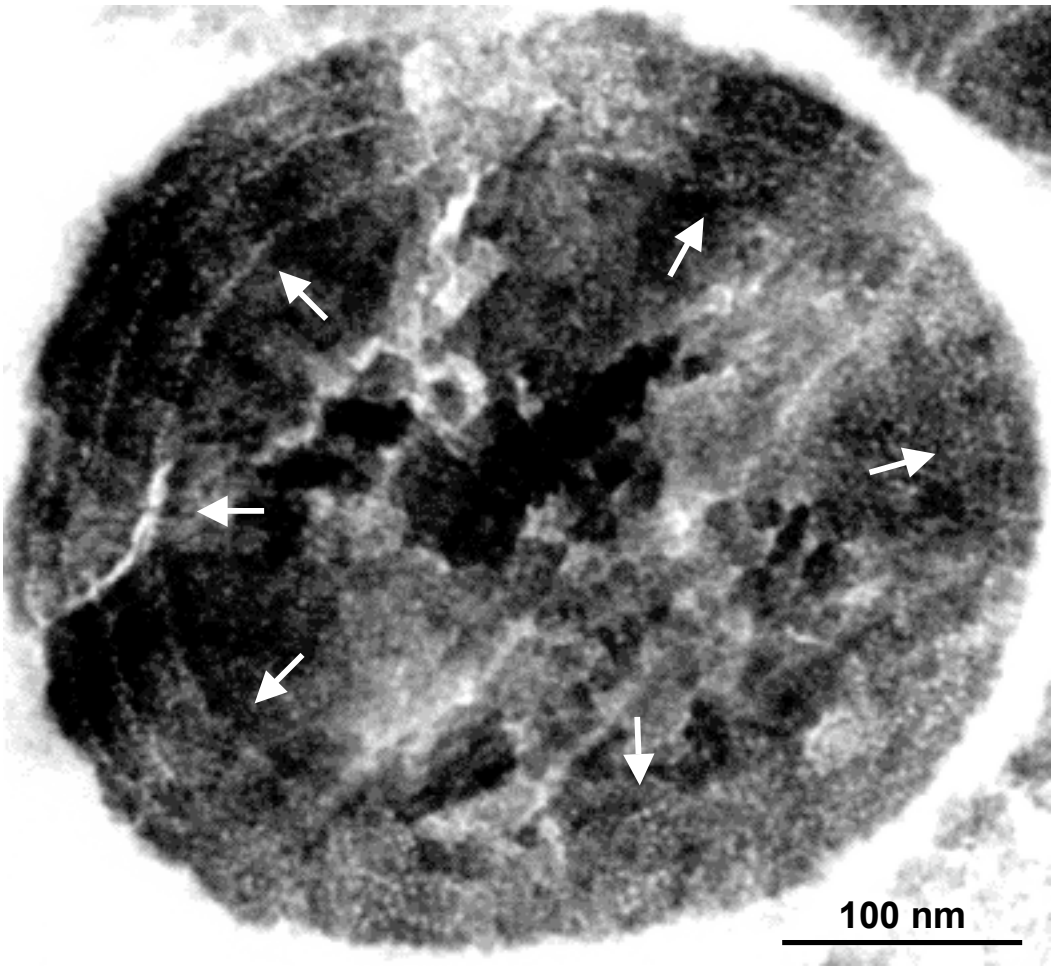

Figure S3

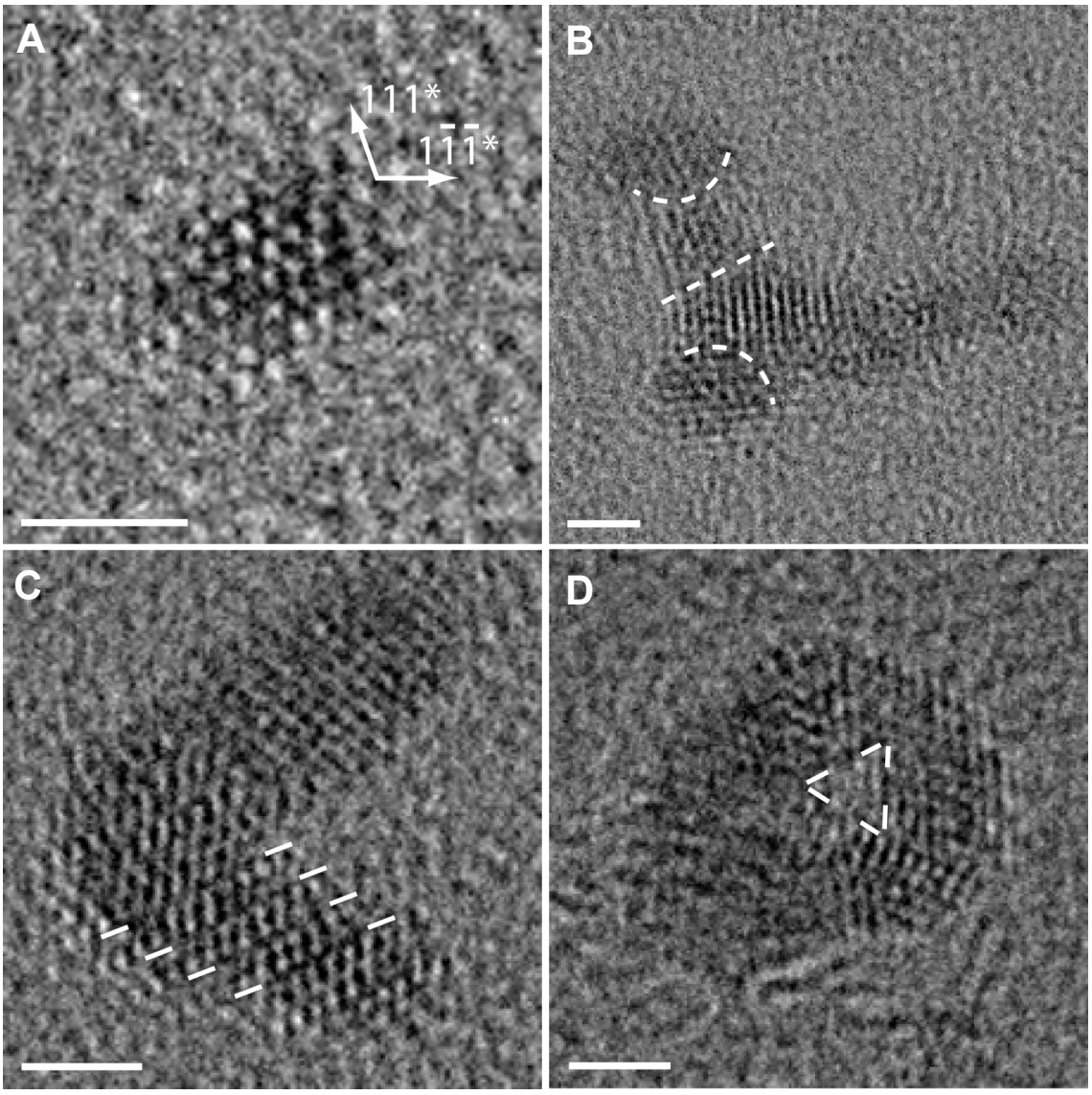

Figure S4

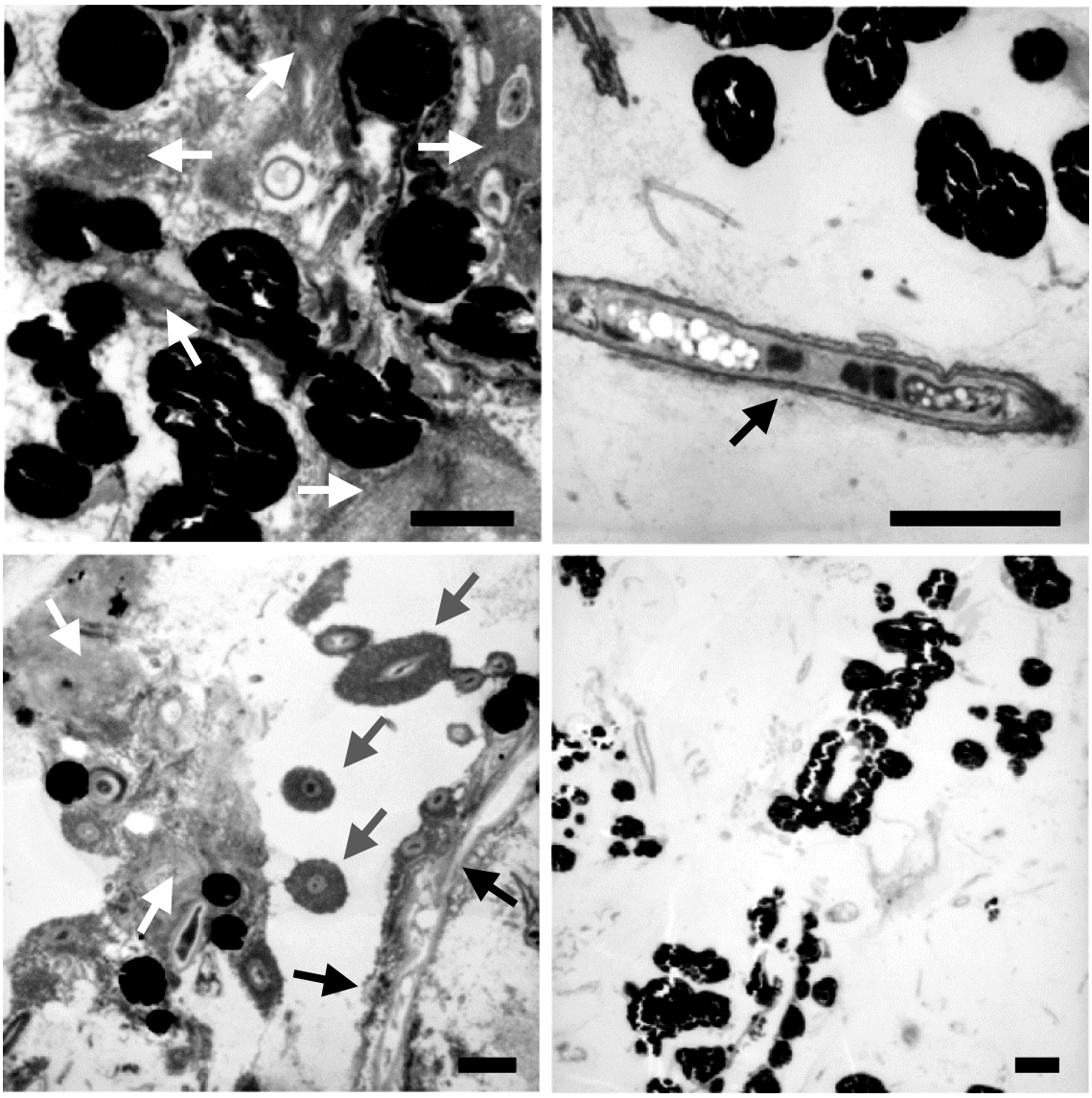

Figure S5

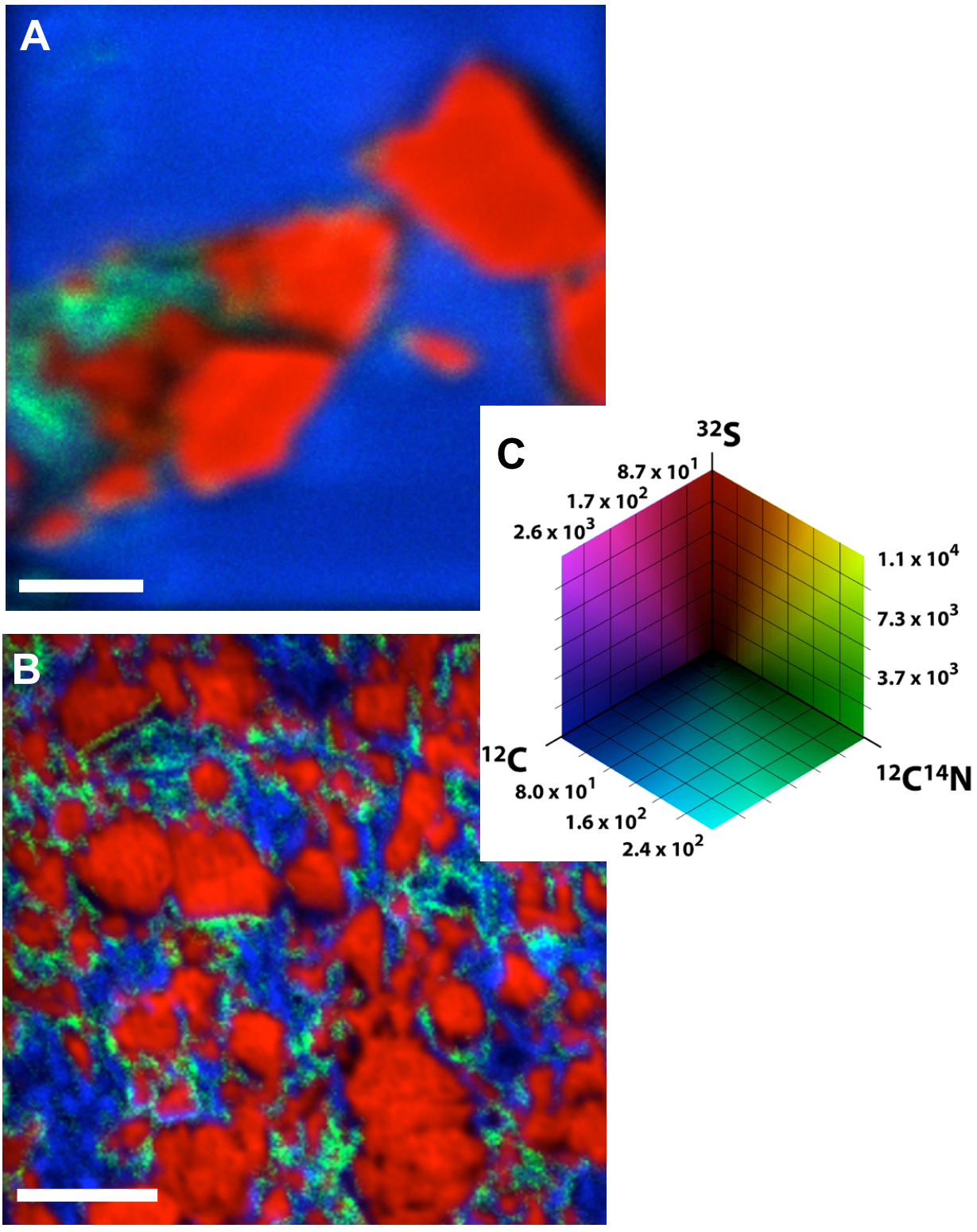
A
B
C
32S
8.7 x 10^1
1.7 x 10^2
2.6 x 10^3
1.1 x 10^4
7.3 x 10^3
3.7 x 10^3
12C
8.0 x 10^1
1.6 x 10^2
2.4 x 10^2
12C14N

Figure S6

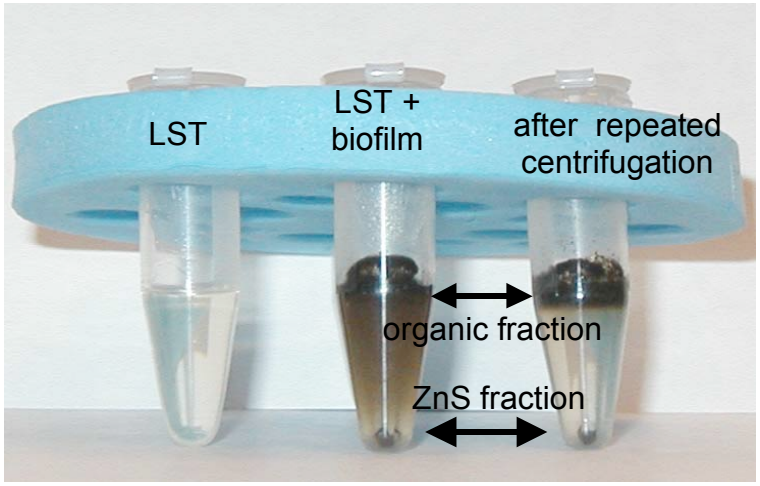
LST
LST +
biofilm
after repeated
centrifugation
organic fraction
ZnS fraction

Figure S7

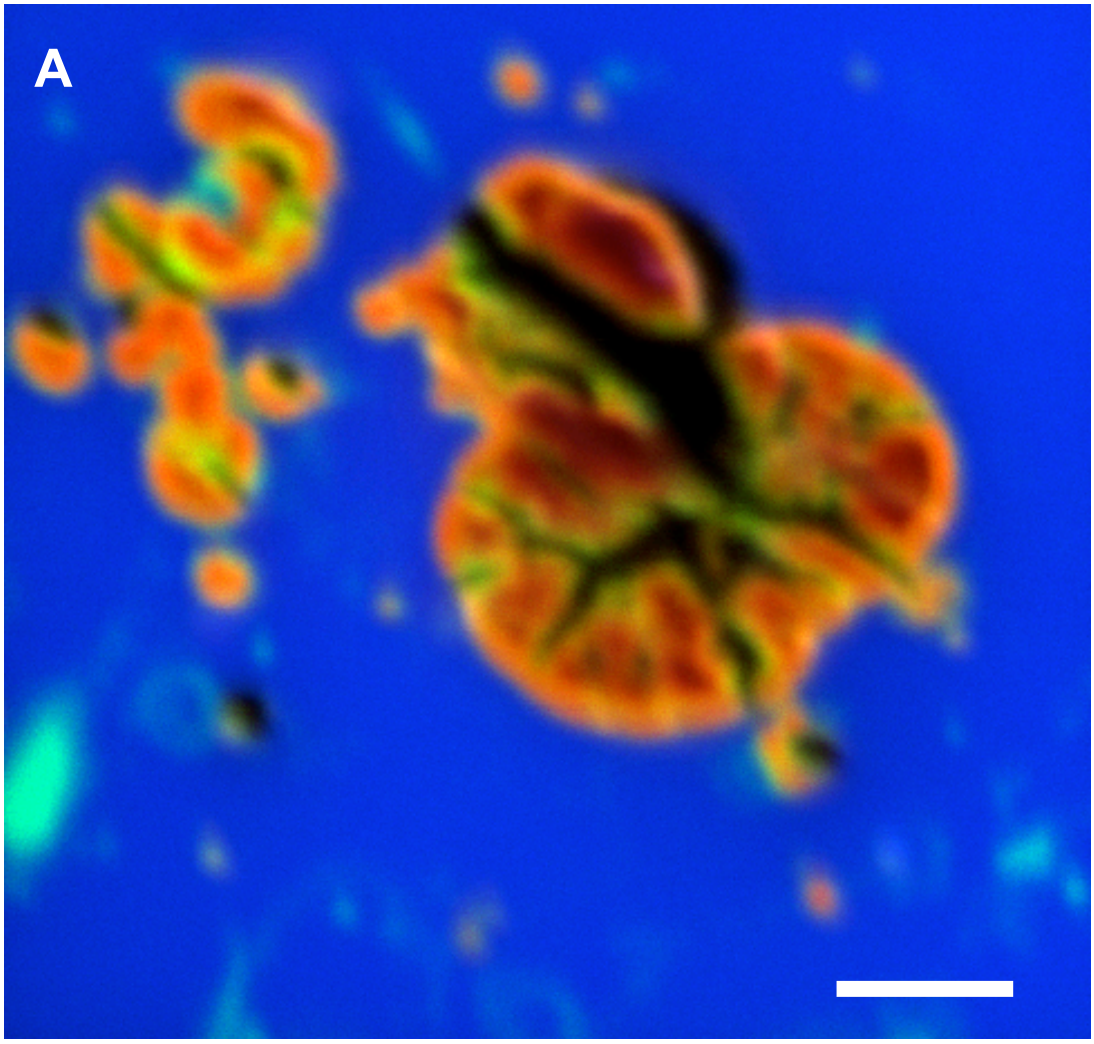
A

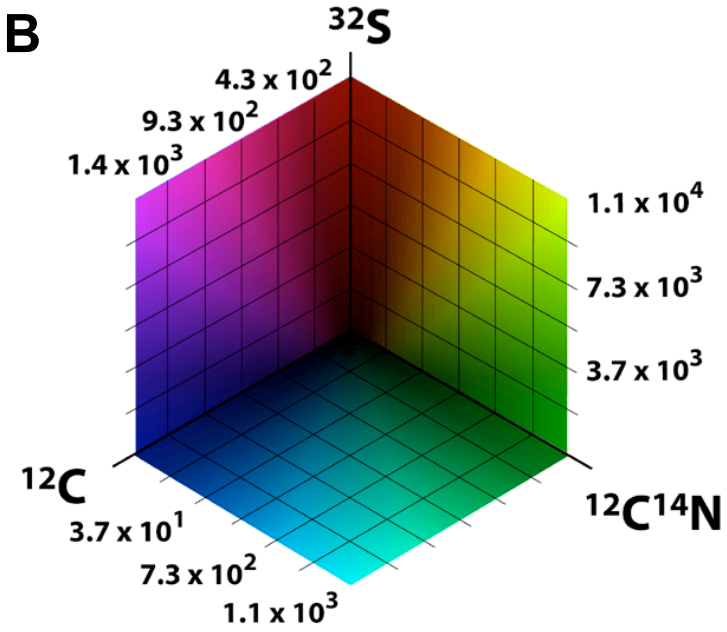
B
32S
4.3 x 10^2
9.3 x 10^2
1.4 x 10^3
1.1 x 10^4
7.3 x 10^3
3.7 x 10^3
12C
3.7 x 10^1
7.3 x 10^2
1.1 x 10^3
12C14N

Figure S7 (cont'd.)

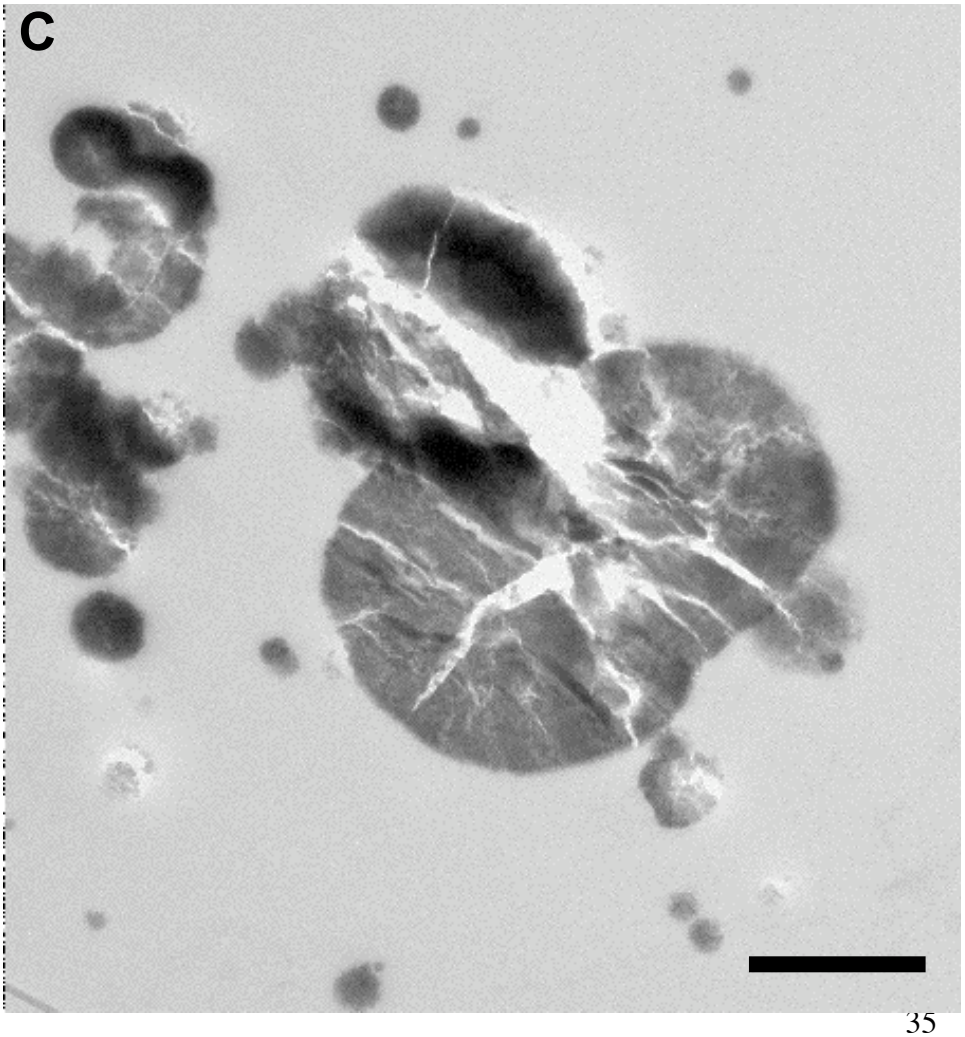

Figure S8

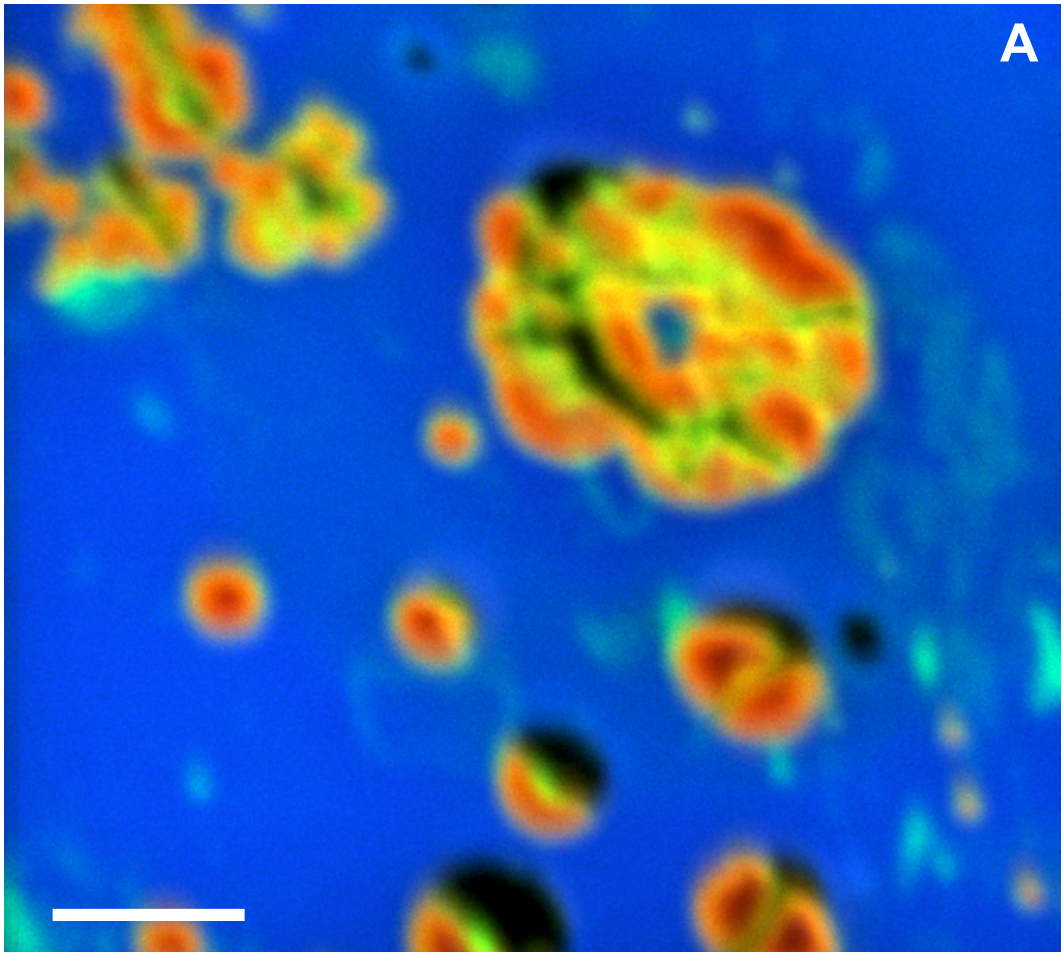
A

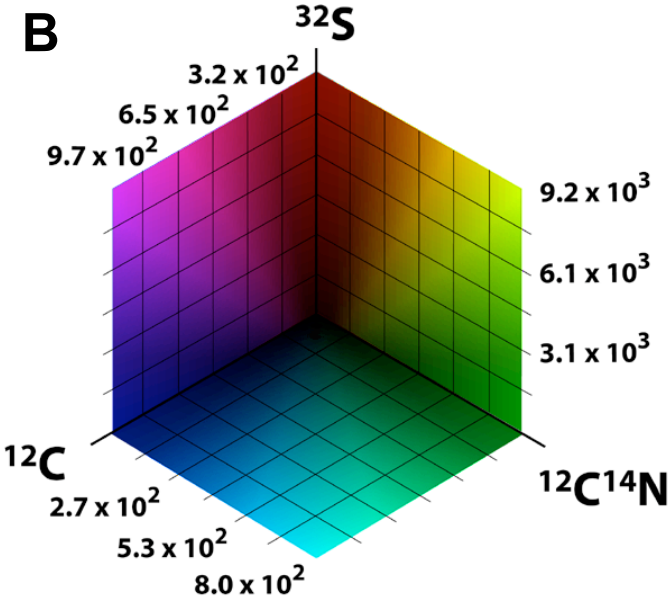
B
32S
3.2 x 10^2
6.5 x 10^2
9.7 x 10^2
9.2 x 10^3
6.1 x 10^3
3.1 x 10^3
12C
2.7 x 10^2
5.3 x 10^2
8.0 x 10^2
12C14N

Figure S8 (cont'd.)

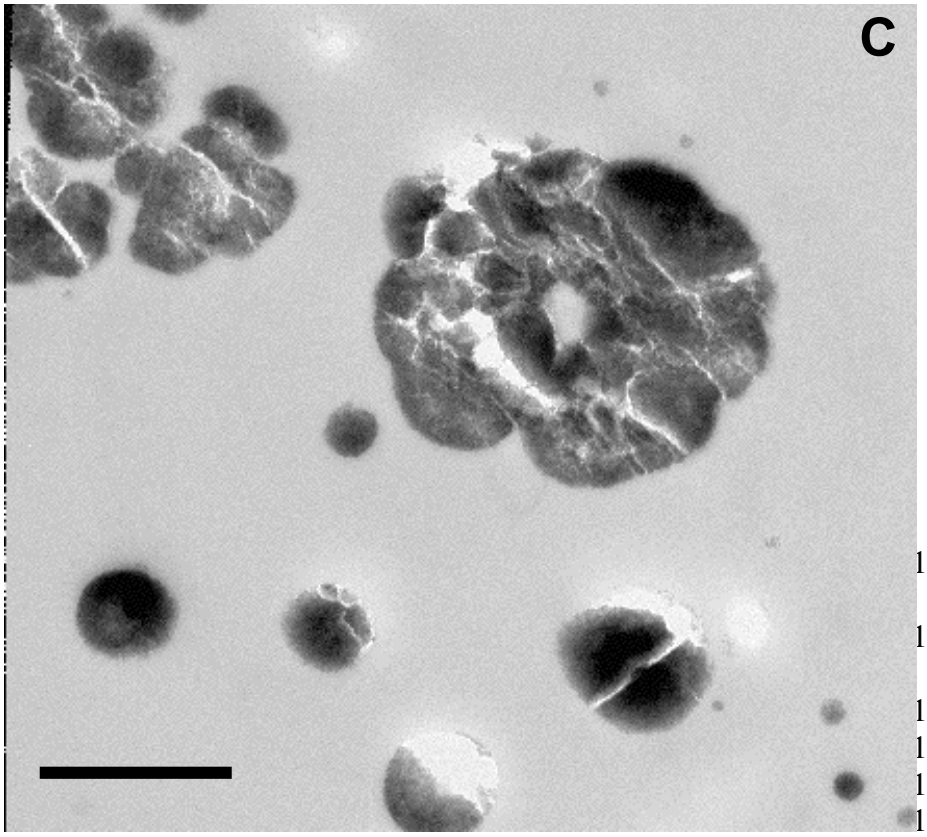

Figure S9

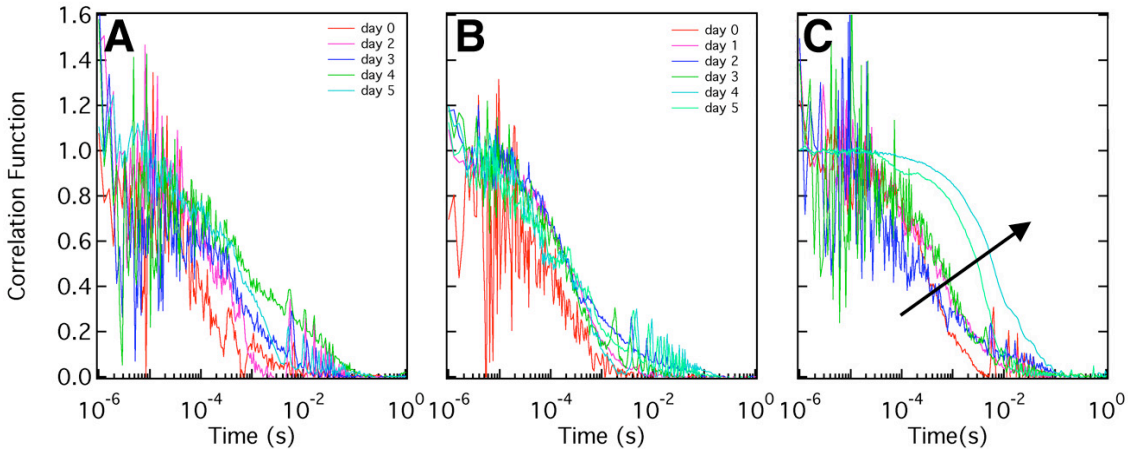
A
B
C
day 0
day 2
day 3
day 4
day 5
day 0
day 1
day 2
day 3
day 4
day 5
Correlation Function
1.6
1.4
1.2
1.0
0.8
0.6
0.4
0.2
0.0
10^{-6}
10^{-4}
10^{-2}
10^{0}
Time (s)
Time (s)
Time(s)